Clogging in Low Reynolds Number Channel Flow

by

Sydney Warren Holway

Thesis Advisers:

Prof. Timothy Atherton

Prof. Jeffrey Guasto

Department of Physics

TUFTS UNIVERSITY

May 2018

1 Abstract

Clogging occurs when particles dispersed in a carrier fluid foul a constriction, interrupting flow. We investigate the regime where geometric effects and not electrochemical attraction between the particles are responsible for the fouling and where fluid flow is at low Reynolds number. To probe the mechanisms behind clog formation, we used high speed video microscopy to observe with sub-millisecond resolution the assembly of particles into a clog. Analyzing the kinematics of the clogging particles reveals the formation of an arch across the channel without prior transition to a dense particle flow state. Differences between the average particle velocity-position profile and the simple incompressible fluid model reveal a local decoupling of the carrier fluid average velocity from the particle average velocity. By correlating the spatial particle distribution and the velocity distribution, we show that local velocity decoupling results from steric exclusion at the channel walls. Prospects for a microscopic model of clogging incorporating these results are also discussed.

2 Introduction

Fouling occurs in suspensions when flow is interrupted by the conglomeration of solid flow constituents. A common example of fouling is blood vessel clotting, in which platelets stick to the walls of a vessel and to themselves, building up to choke blood flow. Clogging is a kind of fouling that occurs in constricted channel flow when the solid constituents of a suspension assemble into a structure that spans the channel diameter and prevents further flow of solids. We refer to this structure as a clog. A clog is not comprised of solids that have become stuck to the channel walls by adhesion, as in the case of clotting. Clogs are stabilized by contact forces between the solids and the walls. This research focuses on clogging in low Reynolds number flow, which means that inertial forces are small compared to viscous forces. We also minimized the electrochemical attraction, including Van Der Waals attraction, between the particles and the walls so clotting is avoided. Such a system is representative of flow

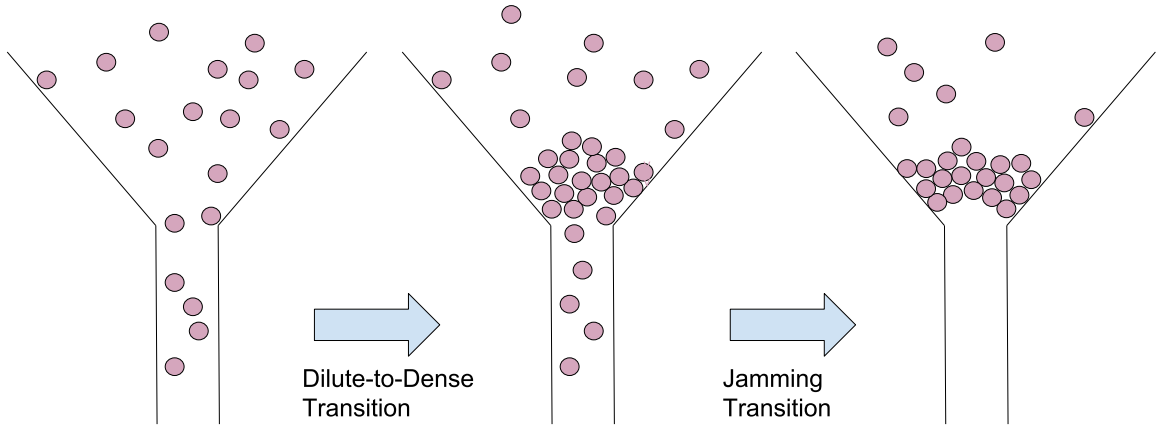

Figure 1: Transition of granular flow concentration from dilute to dense, followed by the transition to the jammed state.

geometries with microscopic length scales, as would exist in fine filtration processes.

A strong motivation for this research is recent progress in the study of jamming in granular flows. Jamming is the sudden arresting of granular flow caused by the assembly of grains into a structure which is stabilized by contact forces. The canonical example of this is a sand pile, but the phenomenon we are observing bears greater resemblance to hopper jamming. When dilute granular flow enters a hopper, inelastic collisions cause energy to dissipate in the hopper inlet. As this energy dissipates from the flow, grains slow down to the point where flow becomes dense (Jie Zhong, 2006). This is referred to as the dilute-to-dense transition (Figure 1).

When the granular flow becomes dense, there is a much higher chance of particles in the hopper to arrange into an arch, which causes the flow to jam. The reason jamming has a higher chance of occurring for dense granular flows can be explained simply if we imagine there are $N = \frac{W}{D}$ specific points existing on an arc line across the hopper, where N is the number of grains required to span the hopper channel, W is the width of the channel, and D is the diameter of the particles. For an arch to develop, a grain must exist at each of the N

specified points in a single frame of time. For higher concentration, there is a greater chance of finding a particle at any point in the flow than there would be in the dilute case, which means that there is a greater probability of finding grains at each of the N points along the arc and hence a better chance of jamming. The configuration of grains into an arch from a dilute flow state would be very unlikely relative to the dense flow case, especially for large throat diameters, and so the jamming transition in granular flow through a hopper almost always follows from the dilute-to-dense transition (Kiwing To, 2005).

Clogging is different than jamming due to the presence of a viscous carrier fluid. For our tests we used 10 μm spherical polystyrene particles suspended in a clotting-resistant carrier fluid, the formulation of which is discussed in section 3. The goal of this research is to investigate the mechanism by which particles clog in two-phase channel flow, as it is currently unknown how clogging occurs and if the clogging transition is similar or not to the jamming transition of granular flow in a hopper.

Sorell Massenburg's paper "Clogging in Parallelized Tapered Microfluidic Channels" divulges research conducted by the Weitz Lab group aimed at investigating macroscopic characteristics of channel clogging. In their experiments, they flowed electrically stabilized polystyrene microspheres through a parallel array of channel constrictions and recorded clogging events for various channel geometries and flow conditions. Their results indicate that clogging probability lessens for smaller channel constriction ratios (channel mouth : channel throat). This is a counter-intuitive result since one would assume in the case of a hopper with granular flow that the wider inlet mouth would catch a greater flow volume of grain, leading to faster jamming (Sorell Massenburg, 2016). The group postulates that the decrease in channel resistance due to the large mouth channel configuration is the cause of the decreasing clogging probability, as higher flow rate would inhibit the stable formation of clots along the channel inlet. The main difference between our experiments and those of the Weitz Lab group is that we choose to prevent clotting using surfactant in our solution. Though clotting is a very important topic of study, we want to observe pure clogging that

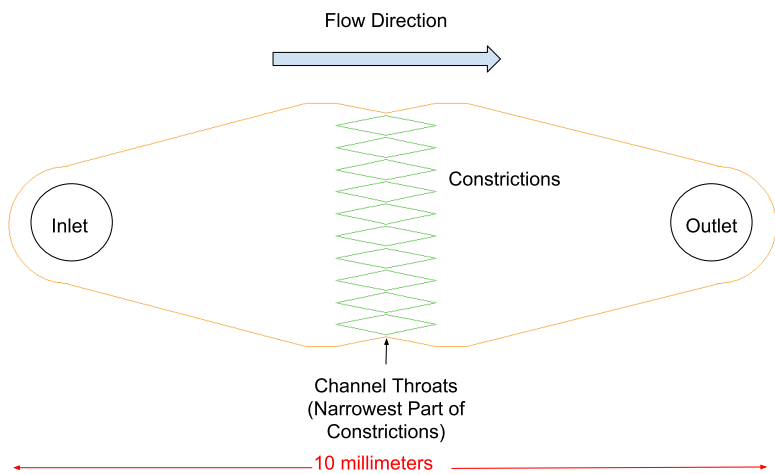

Figure 2: Microfluidic device design. Flow passes through a parallel array of channel constrictions, which narrow from 300 μm in width at the mouth to 30 μm at the throat. The device design itself is in yellow and green, while the annotations are in black and red.

does not result from sticking. In regards to analysis, the novelty in this research is that we explore the micromechanical characteristics of clogging by probing mechanisms behind clogging transitions.

3 Methods

To induce clogging, we designed microfluidic devices with a series of parallel constricted channels (Figure 2). The parallel arrangement allows for constant flow velocity through each channel during pressure driven flow, which is important if one or more channels become fouled during the course of an experiment. This feature also.enables us to view multiple clogging events during a single test.

We used particles with a diameter of $D = 10$ μm, and so the width of the channel constrictions narrow from 300 μm at the mouth to $W = 30\mu$m at the throat, giving a constriction ratio of 10. A 30 μm throat width avoids filtering, which happens when a particle is simply too large to fit through the channels. We drew this 2D design in AutoCAD and colored the different layers to clarify which sections are open and which are solid, then

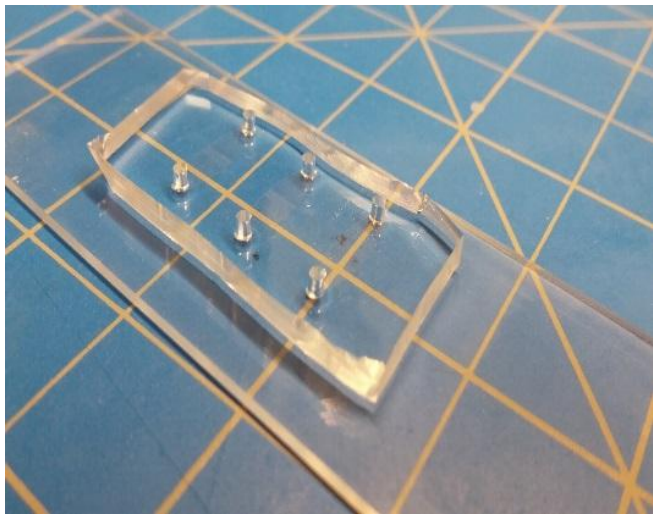

Figure 3: The completed microfluidic device consisted of a PDMS channel bonded to a microscope slide. This design allows us to observe channel clogging.

sent the design to a facility where they laser cut a mask for the design. We then used photolithography to to transfer the mask onto photoresist on a silicon wafer. At this stage, controlling the depth of the photoresist layer was paramount: the microfluidic channels needed to be shallow enough so that the particles form a monolayer as they clog, but deep enough so that particles don't become stuck between the floor and the ceiling of the channel during flow. Given that photolithography is only accurate to within several microns for the spin coating, we aimed for an $H = 15\mu$m channel depth so that $H/D = 1.5$. The etched wafer served as a mold in the final step of the fabrication process. We used soft lithography to mold slabs of PDMS (polydimethylsiloxane) inlaid with our designs. We then plasma bonded these PDMS slabs to microscope slides to produce the final devices which would be used for experimentation (Figure 3).

To set up for an experiment, we placed our microfluidic device on a Nikon Ti-e microscope and focused on the channel constrictions with 10x magnification. Instead of looking through the microscope eyepiece, we observed our channels using a high speed camera mounted on the c-mount port of the microscope. We checked for any fabrication anomalies that could

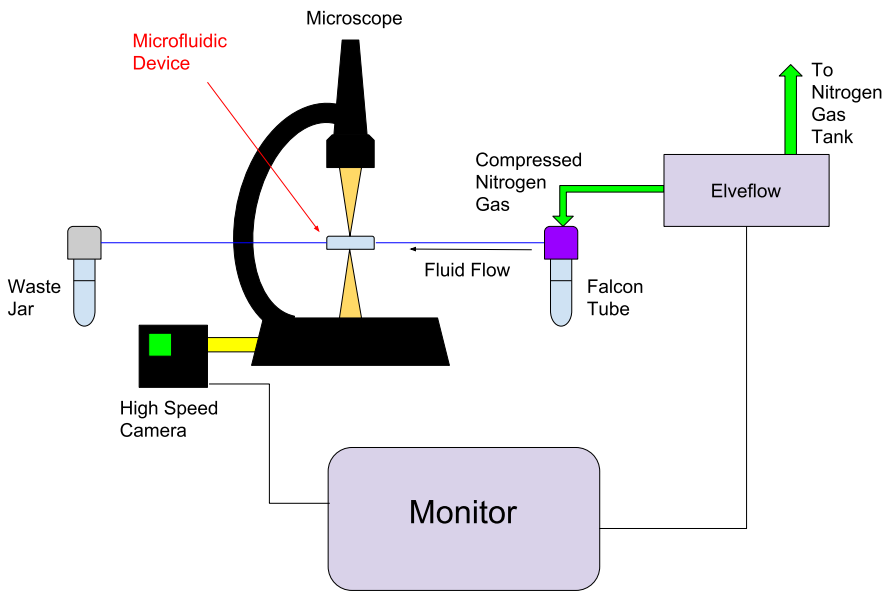

Figure 4: Experimental Set-up

ruin the experiment, such as fused channels or gaps in the seal between the glass and the PDMS.

Next we mixed a particle solution. Upon choosing a device for testing, we inserted an inlet tube into one end of the device and fed it into a Falcon tube. On the opposite end of the device, we inserted an outlet tube and fed it into a waste jar. We pressurize the falcon tube to 40 mbar with a nitrogen gas hose fed through an Elveflow OB-2 microfluidic flow controller. The Elveflow allows us to quickly monitor and adjust fluid pressure (Figure 4).

When running the experiment, we first inject 1 ml of particle-free media into the Falcon tube and drive it through the channels. It is important to run media before particles so that any initial air bubbles that enter the system have time to flow out into the waste jar. When the Falcon tube is just about empty, we inject the particle-laden solution. Setting the frame rate to 10,000 fps, we watch the particles flow through the device and record a video when we see a channel become fouled. It is important that the camera is set to

"end-trigger" mode, which means that the camera is continuously recording and overwriting previous footage. When "record" is pressed in end trigger mode, the camera saves all the current memory, which is the last 2 to 8 seconds of footage depending on frame rate and window size. When we capture an event, we shut off the flow and upload the video from the camera to an external drive, then we resume flow and repeat until all of the channels become fouled and the device is no longer usable.

The greatest difficulty in designing our experiment was determining how to formulate our particle solution. We narrowed down the formula through trial and error, starting with the particles themselves. To choose the particles which would suit our experiments, we considered how electrostatic interactions would affect the ability of the particles to clog. Since chemical adhesion is not present in the clogging regime which we wish to study, we needed to minimize the electrochemical attraction between the particles and the walls of the microfluidic channel. PDMS carries a net negative surface charge in water, and so we choose to use 10 μm diameter carboxylated polystyrene latex microspheres (MAGSPHERE catalog no. CA010UM), which would be weakly repelled by the PDMS channel due to the negative charge of the surface carboxyl groups. We ran our first clogging test with a dilute solution of carboxylated polystyrene microspheres, and were surprised to see that our device quickly fouled due to particle-particle and particle-wall adhesion (Figure 5).

The tendency of our particles to stick despite their net electrostatic repulsion is explained by DLVO theory, which defines a zeta potential between two particles as the sum of their electrostatic repulsion and Van Der Waals attraction. For our particles in solution, the electrostatic component of the zeta potential does not obey coulomb's law due to the screening effect of ions present in solution. Instead, a double layer of coions and counterions form around the particles, and it is the repulsion between the counterion clouds which causes a positive interaction potential between particles (Zeta-meter inc.). The Van Der Waals interaction is a sum of dipole and dispersion forces between molecules that is, for separation

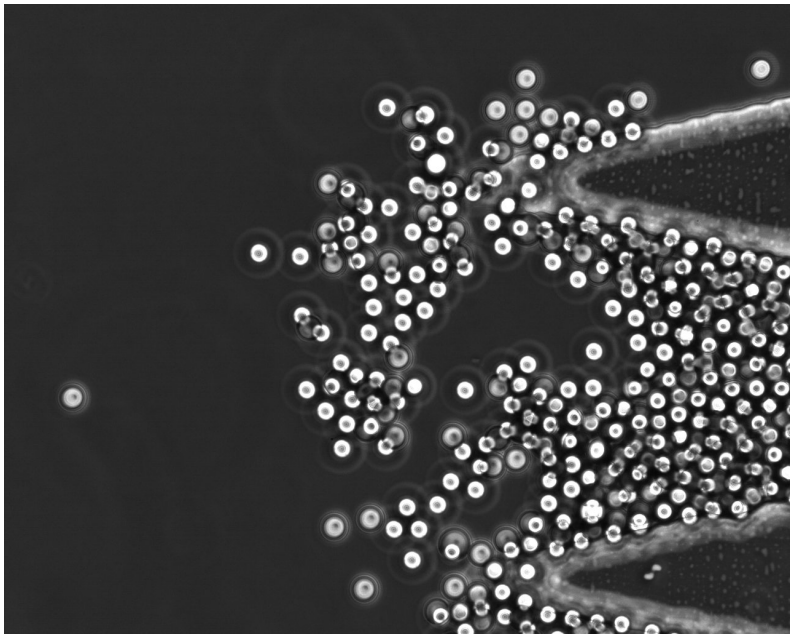

Figure 5: Particle-particle and particle-wall sticking lead to undesirable clotting on the channel walls.

distances $R << D$, approximately inversely proportional to the separation distance R (Hugo Hamaker, 1937). For the case of two large spheres at small separation distances, the double layer electrostatic potential W_e and Van Der Waals potential W_v take the following form:

$$W_e = Ae^{-kR}$$

$$W_v = -B/R$$

A, B and k are determinable constants while D is the separation distance between two interacting spheres. Summing these two potentials results in the zeta potential, which shows roughly how particle attraction changes as a function of separation (Figure 6).

The problem when we were flowing carboxylated particles in water was that the kinetic energy of the particles was sufficient to overcome the initial repulsion of the zeta potential, causing them to become stuck to one another in the primary minimum. This theory also

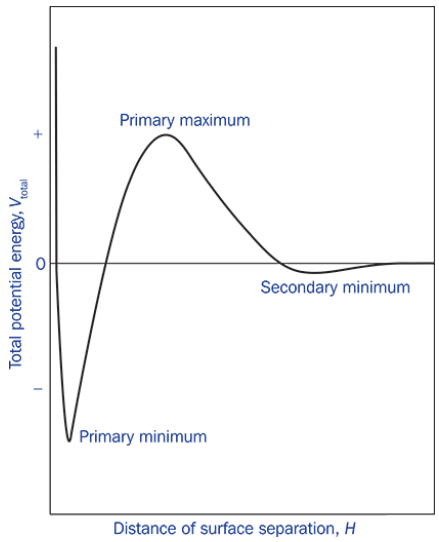

Figure 6: The zeta potential for two interacting spheres exhibits a local minimum at small separation. Reprinted (Behzad Vaziri Hassas, 2013)

explains why particles tended to stick only when they came in contact with the channel walls or with already stuck particles - the kinetic interaction between particles is a function of their relative velocities, and so it would be unlikely for two free flowing particles to become stuck to each other. We decided to combat the problem of sticking by adding the surfactant TWEEN 20. Surfactants are large molecules that are hydrophobic at one end and hydrophilic at the other. The purpose of adding TWEEN 20 to our particle solution was so the hydrophobic heads of the molecules would attach to the surface of the particles and to the walls of the channel, with the hydrophilic tails extending outward. The hydrophilic layers would then act as a barrier keeping coated surfaces from coming in close enough contact to fall into the zeta potential minimum. Running flow tests with TWEEN 20 added at CMC (critical micelle concentration) to the particle mixture resulted in an apparent reduction of sticking. The CMC of TWEEN 20 is 60 mg/L, above which the TWEEN 20 molecules may assemble into independent structures such as micelles, liposomes and bilayer sheets. In order to qualify the effects of using carboxylated particles and adding TWEEN 20 to our particle solution, we devised a test to ascertain the susceptibility to fouling for our different mixtures. Using solutions of carboxylated and non-carboxylated polystyrene microspheres

with various concentrations of TWEEN 20, we filmed channel flow for 20 seconds, counting from when liquid first entered the microfluidic device, and then took a snapshot of the channel. Comparing the degree of clotting in each of the snapshots revealed relatively how sticky the particles were in each of the solutions (Figure 7).

The chart shows that the least amount of sticking occurred with carboxylated particles in a solution supersaturated with TWEEN 20. Ordinarily, increasing the TWEEN 20 concentration beyond the CMC should not lead to less sticking because all surfaces should be fully coated in a layer of molecules before micelles start to form; increasing concentration should only create more micelles. The decrease in particle sticking in a supersaturated solution of TWEEN 20 indicates that the additional surface area presented by the particles slightly increases the effective critical micelle concentration, and thus a higher concentration of TWEEN 20 is required for all surfaces to be fully coated in surfactant.

For the concentration of TWEEN 20 to use in our clogging experiments, it would be trivial to choose the 2% concentration which performed well in the sticking test. However, a high concentration of surfactant can cause the fluid to have a nonlinear rheology due to the presence of large micellar structures. To avoid complicating our analysis, we decided to increase the TWEEN 20 concentration in our particle solution to only twice CMC, which is high enough to passivate the surface of the particles and low enough so that the carrier media still behaves as a simple fluid.

With a solution of particles that exhibits very little particle-particle and particle-wall sticking, one lingering problem to assess was the tendency of particles to drag along the floor of the microfluidic channel. This occurred because the density of our particles was 1.05 g/ml, causing them to sink in water. We used glycerol to density match the carrier media with the particles, assuming a linear relation between density and glycerol concentration. The actual density of our solution when density matched using this assumption can be determined

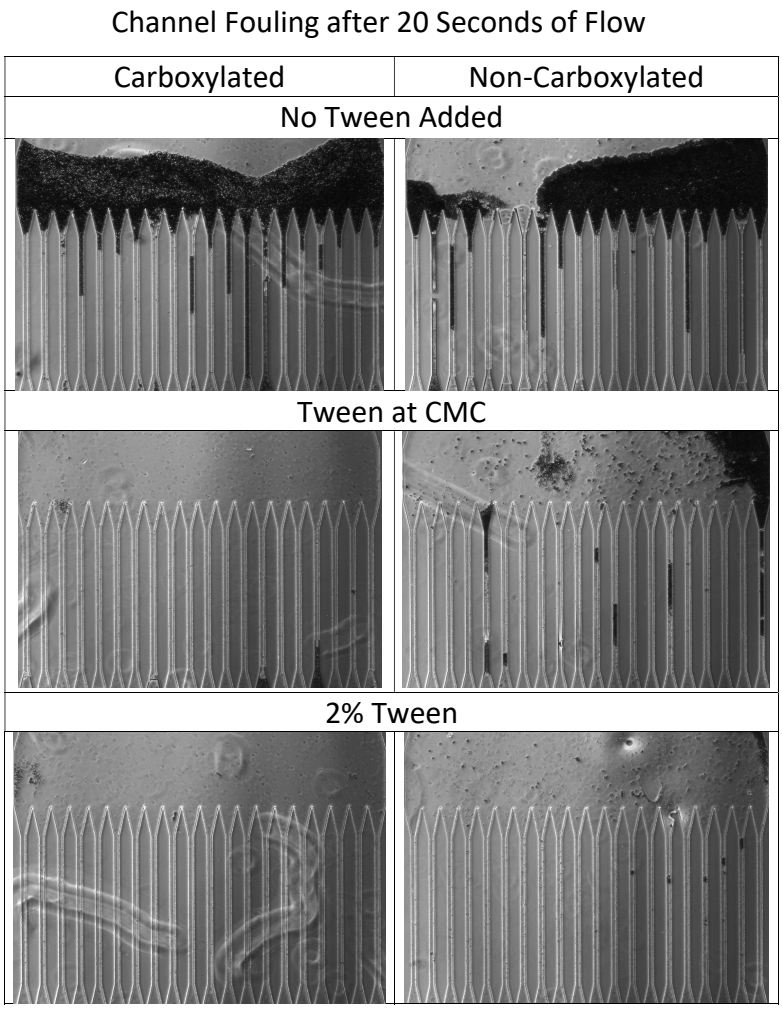

Figure 7: Sticking tests confirm that high TWEEN 20 concentration and the use of carboxylated particles significantly reduces sticking. This channel design differs from the one used in the final clogging design because an older microfluidic device was used to conduct the sticking test.

from a glycerol table to be 1.044 g/ml using density values listed under 15 degrees Celsius. We determined this discrepancy to be negligible by calculating the settling velocity of our $\rho_p = 1.05$ g/ml particles in a $\rho_f = 1.044$ g/ml solution:

$$v_{settling} = \frac{2(\rho_p - \rho_f)g(D/2)^2}{9\mu_w} \cong 1\mu\text{m/hour}$$

Here $\mu_w = 1.1$mPa·s is the dynamic viscosity of water, the use of which causes an overestimate for the settling velocity since our glycerol-water solution would have higher dynamic viscosity. From later mentioned analyses, the slowest free flowing particle velocity in our device is at least about 10 mm/s. This means that the longest time a particle spends in the microfluidic device is $\tau = 1$s, over which the particle falls a distance of $d_{max} = v_{settling}\tau =$ 0.3nm. Given that d_{max} is orders of magnitude smaller than the radius of a particle, it is safe to use our naive density matching method, for settling will not occur during the course of an experiment.

Despite our best efforts with the optimal particle solution, we found it difficult to capture high speed videos of clogs in our current microfluidic devices. This difficulty partly resulted from trouble in timing our videos. Recording at 10000 frames per second, the minimum rate necessary to analyze our videos, the camera only had enough memory to store the last 2 seconds of footage shot. When fouling occurred in the device, it was unclear whether the fouling was due to clogging or dust contamination. In the time it took to record a video once fouling occurs, navigate through the frames to determine if the event was captured, and save the footage to an external drive, many other channels had already fouled in our device. So, for one experiment, even though there are many clogging channels built into each device, we could only record one or two fouling events per experiment. Cutting off flow in between recordings only slightly helped with this problem because sudden back flow also induced channel fouling. The inability to record many fouling events per test was a major problem because most fouling events we witnessed were due to large clots of fused particles or dust

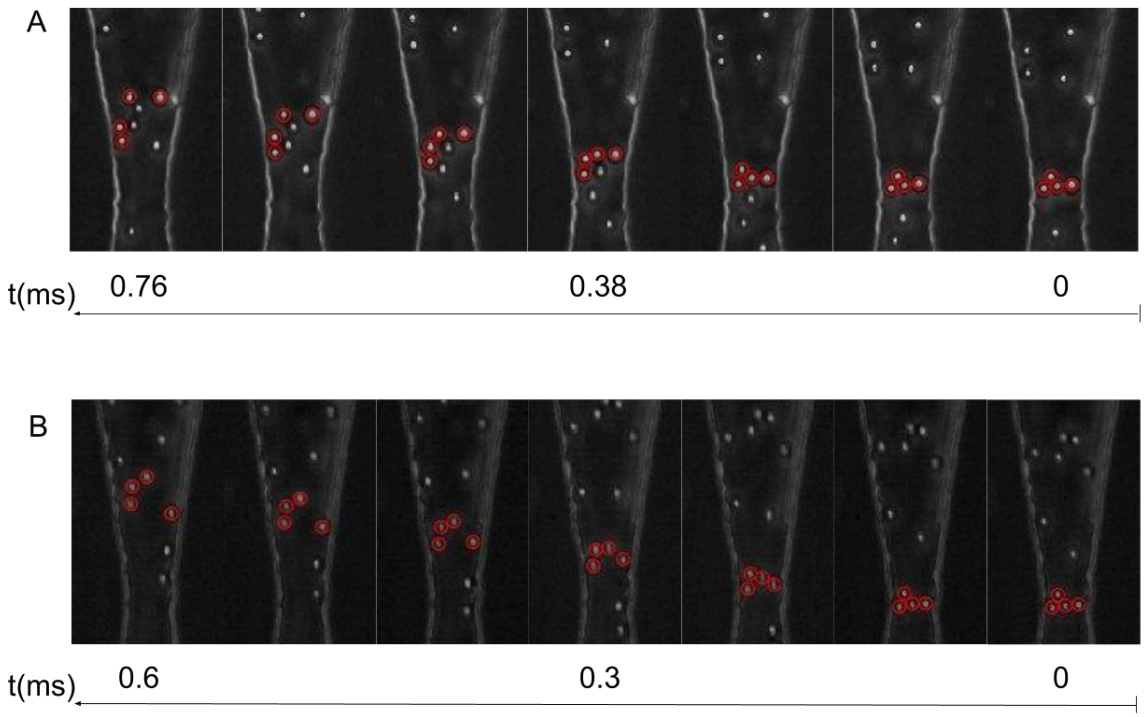

Figure 8: Image sequences of clog formations. A is clog 1 and B is clog 2. Clogging particles are outlined in red. The time scale at the bottom of each sequence shows the length of time remaining before the clog occurred.

lodging in the throat of the channel. Nevertheless, we were able to improve the cleanliness of our procedure to reduce the chance of dust entering the flow, after which we finally recorded clogging.

4 Analysis

Having developed a robust procedure for observing adhesion-free flow, we recorded a total of two clogging events. With our current procedure, we've been able to record a true clogging event once every three experiments, so we expect to be able to showcase a larger sample size in future work. The following frame sequences show how the two clogs had formed (Figure 8).

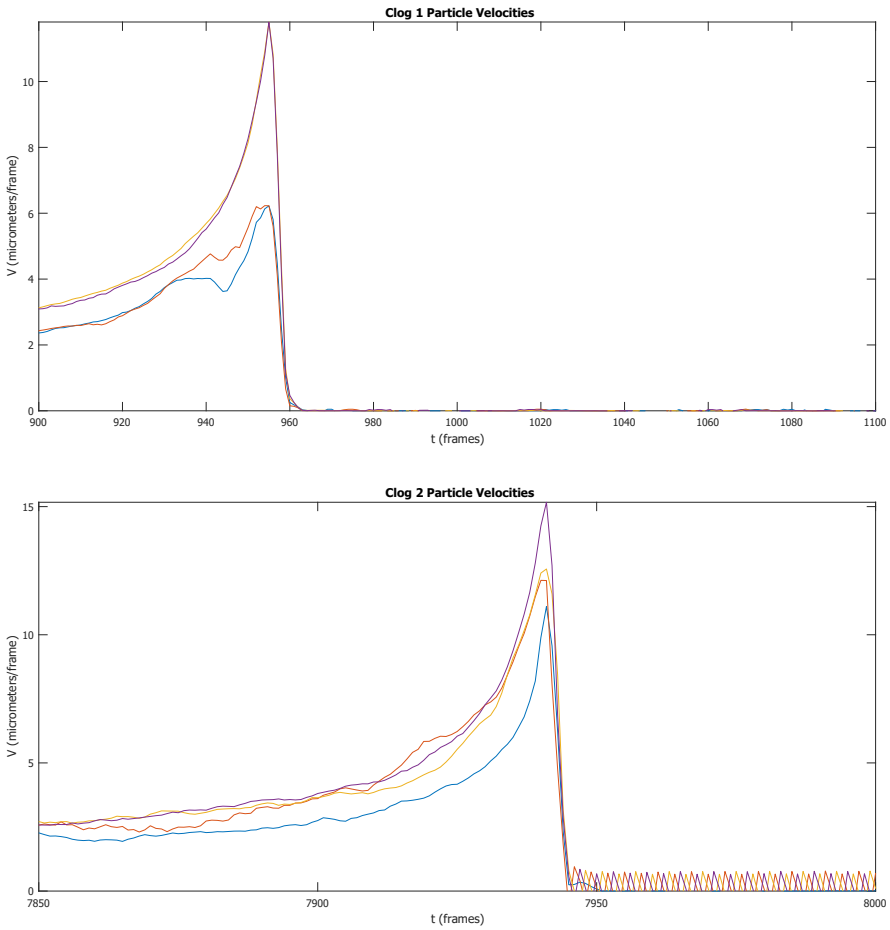

Figure 9: Velocity-time graphs of the two clogging events.

Neither of these clogs formed from a dense state, as in the case in granular hopper jamming. They formed from a dilute flow state when the positions of 4 particles were drawn into an arch configuration at the throat of the channel. Studying the velocity-time graphs of the particles involved in each of the clogs reveals that all particle-particle and particle-wall contact occurred simultaneously to result in arch formation (Figure 9).

We had initially hypothesized that clogging would occur in a similar manner to hopper jamming, with a transition to a dense flow state precluding the development of a clog. As in the case of hopper jamming, we thought that a dilute-to-dense transition would occur as a result of particle energy losses at the channel walls due to friction. To see how two-phase

flow is affected by the presence of channel constrictions in our set-up, we examined how the particle flow velocity and concentration changes along the length of the channels. For subsequent analysis, y is the flow direction, increasing in the direction of flow, and v refers to the velocity component in the y direction (Figure 10).

Our tracking algorithm generates a list of tracks with the position and velocity vectors of each particle that passes through our analysis region. A scatter plot of the v-velocity and y-position vectors for each particle track reveals the expected broadening of the velocity distribution range as flow velocity increases near the channel throat (Figure 11).

One key feature of this graph is the lack of data points near zero in the vicinity of the channel throat. This illustrates an important distinction between the motion of the particles and that of the carrier fluid. While the velocity of the fluid approaches zero near the channel walls, there is a minimum velocity at which the particles can travel due to their finite size. Roughly approximating that the particle velocity is equal to the expected fluid velocity at the particle center, the slowest a particle in free flow can travel is the expected fluid velocity at 1 particle radius away from the channel wall. The actual minimum velocity may be less if friction effects are significant. The steric effect which excludes particles from inhabiting the lowest velocity regions of the flow field causes the development of a bimodal particle velocity distribution as the flow constricts (Figure 12). Given the high aspect ratio of our channels, we would expect a simple fluid to exhibit Hele-Shaw flow, wherein the mean velocity is very close to the max and the velocity distribution is J-type (peak on the higher end with a tapering tail on the left). This J-type distribution is clearly exhibited by the particles as well for much of the channel inlet, but subsides towards the channel throat.

The growth of the lower peak of the velocity distribution results from the collection of particles to the edge of the channel. This collection is due to the nature of the particles in low Reynolds number flow to follow their pathlines. As the pathlines condense towards the throat of the channel, the distance between one particle's streamline and the channel wall

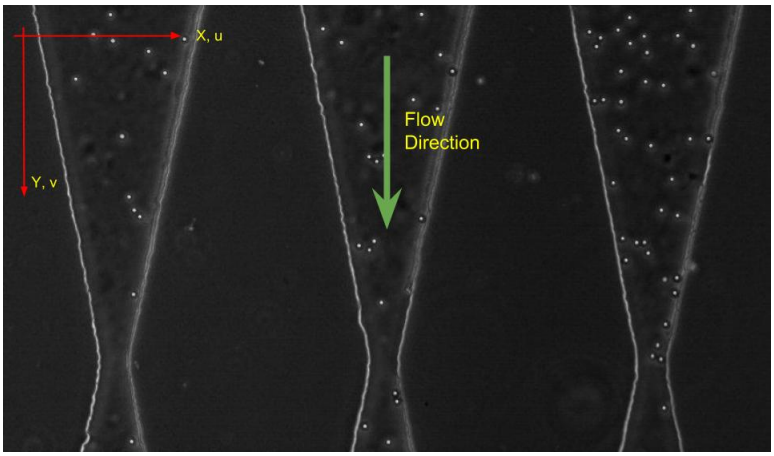

Figure 10: Particles that flowed through this region were tracked to obtain statistics on how a constriction affects particle concentration and particle velocity.

diminishes until it is equal to the radius of the particle, after which the particle is forced into a higher velocity region of the flow field. By this effect, a large portion of the particles entering the channel constriction end up in contact with the wall, as is shown by the particle number density plot (Figure 13). We hypothesized that the collection of particle velocities to the edge of the channel causes a decoupling between the average fluid velocity and the particle velocity since particles that would otherwise inhabit a slower velocity region of the flow field are forced into a higher velocity region.

To gauge the effect of particle collection at the walls on the average velocity of the particles, we compare the measured average particle velocity to a prediction based on the simple incompressible fluid model. We are not predicting the velocity of the carrier fluid in the channels, we are predicting how the velocity of the particles changes approaching the constriction throat by assuming the particle flow behaves as a simple fluid flow. By taking the particle velocity at the beginning of the channel as v_0 and the depth of the channel D to be constant for all x and y, we can predict the change in fluid velocity using continuity.

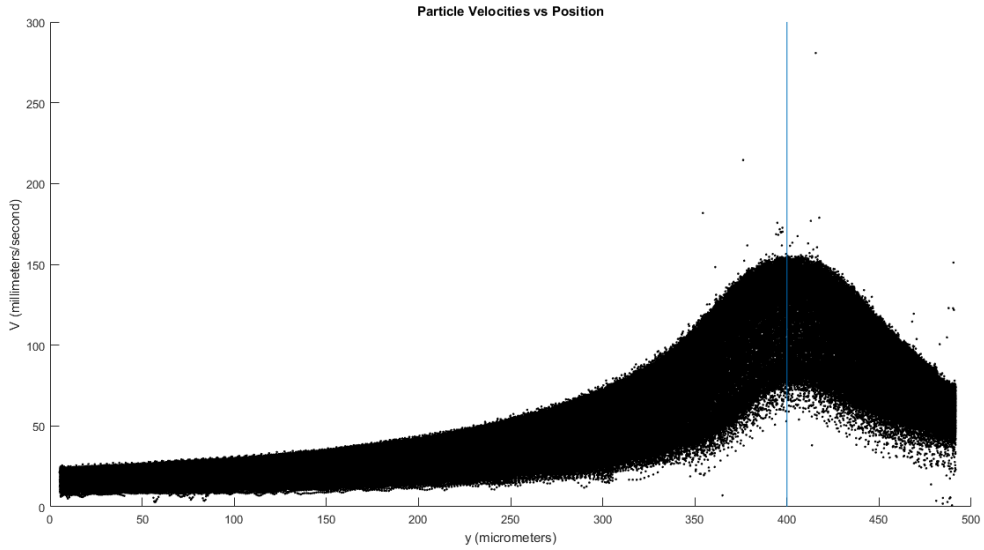

Figure 11: As particles approach the channel throat center (y = 400) velocity increases and the distribution range increases. There are a few outliers in the higher velocity region due to the higher chance of tracking error. The blue vertical line indicates y-position of the center of the channel constriction throats for this and subsequent figures.

$$\Phi_0 = \Phi(y)$$

$$\int_x v_0(x)da = \int_x v(y,x)da$$

$$D\int_x v_0(x)dx = D\int_x v(y,x)dx$$

$$(\Delta x)_0 D(1/(\Delta x)_0)\int_x v_0(x)dx = (\Delta x)_y D(1/(\Delta x)_y)\int_x v_0(y,x)dx$$

$$A_0 < v >_0 = A(y) < v > (y)$$

$$A_0 V_0 = A(y)V(y)$$

For readability we have replaced $< v >$with V. Given that D is constant, we may can

go a step further to show that average velocity V is inversely proportional to channel width Δx.

$$(\Delta x)_0 D V_0 = (\Delta x)_y D V(y)$$

$$(\Delta x)_0 V_0 = (\Delta x)_y V(y)$$

Vy can now be calculated anywhere using the initial average particle velocity V_0 and knowing the width of the channel $(\Delta x)_y$. Since the channels did not come out with the exact dimensions or precise lines that we had drawn for our designs, it was necessary to determine the channel width through image analysis. Taking the derivative of the minimum image of our channels and thresholding above a tuned brightness value yielded choppy lines at the channel walls. By taking the x-axis difference between consecutive wall lines and filling in the gaps with linear interpolation, we obtained a very accurate measure for the channel width as a function of y (Figure 14). The width does though need to be reduced slightly so that the minimum width is equal to 31 μm (our measured value for the average width across the channel throats), because the bright reflection of the channel walls in the camera caused our differential analysis scheme to slightly overestimate channel width by creating peaks roughly 1 μm into the channel wall.

The slightly jagged nature nature of the width function is partially resultant from the analysis method, but tolerable considering that prevalent bumps and features are due to imperfections of the channels themselves. Using this width function, we add our velocity prediction to a plot of the average measured particle velocity (Figure 15). The average measured velocity is obtained by binning the y-axis of the channels into 6 μm bins and taking the average of the velocities found in each bin. Comparing the simple incompressible fluid model with the average measured particle velocity reveals a slight velocity decoupling as particles approach the channel throat at y=400, with the average velocity of the particles

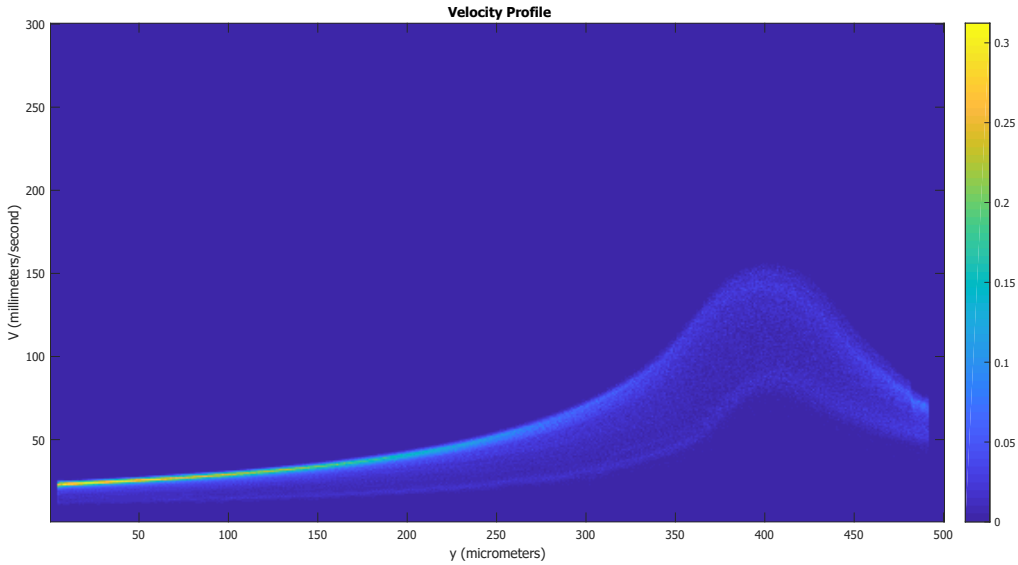

Figure 12: Particle velocity distribution normalized by number of counts in each y bin. Approaching the channel throat, the strong peak on the high end of the velocity distribution subsides as a secondary peak at the low end of the velocity distribution emerges.

rising above the model prediction. Right at the center of the channel throat, the simple fluid model prediction seems to slightly surpass the average particle velocity, which causes a discrepancy in later analysis, but this bump is likely the result of bin averaging. At y=400, where the particles are flowing the fastest, averaging over width of the y-bins tends to artificially flatten the velocity profile.

Since the simple fluid model is designed around the incompressibility constraint, the differences between the model prediction and the measured average particle velocity would seem to suggest either compression or expansion of the particle flow. This assertion can be tested by modelling concentration as a function of the discrepancy between the simple fluid model and the measured velocity and comparing the prediction to the actual change in concentration. The concentration prediction may be derived from the particle flux balance. Here I shall refer to the measured initial particle concentration as C_0, the initial measured average particle velocity as V_0, and the initial area as A_0. On the right hand side of the

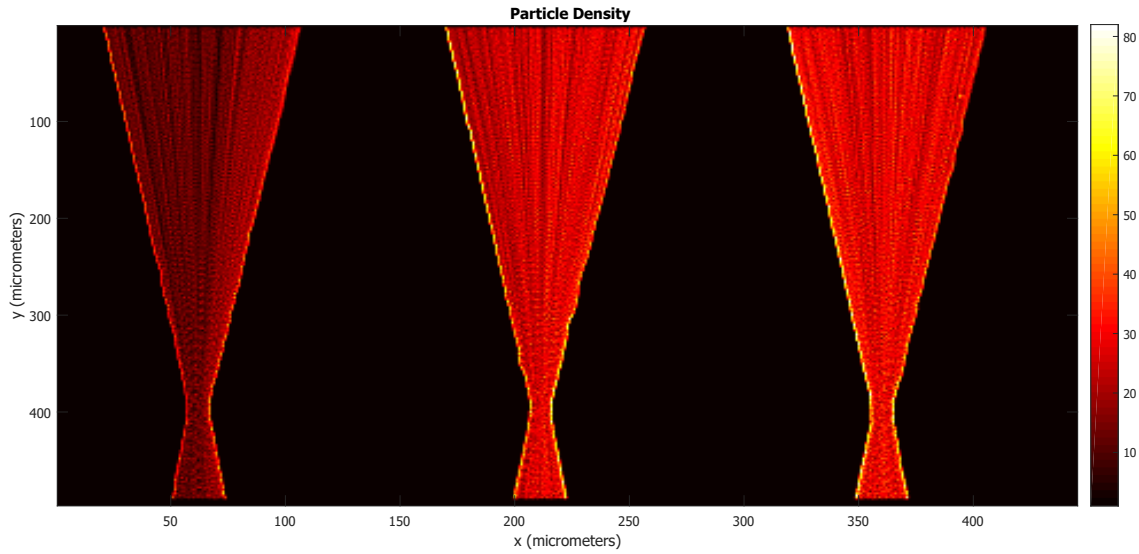

Figure 13: Density plot of the particles in the channel constriction summed over all frames. Significant particle collection occurs at the walls of the channel.

first equation below, we have the area at point y $A(y)$ and the measured particle velocity at point y $V(y)$. $C(y)$ is to be solved for in terms of $V(y)$, C_0, and the simple fluid velocity prediction $V_s(y)$.

$$C_0 A_0 V_0 = C(y)A(y)V(y)$$

$$C(y)/C_0 = (A_0/A(y))(V_0/V(y))$$

$$C(y)/C_0 = (V_s(y)/V_s(y_0))(V_0/V(y))$$

For a reference point of our simple fluid model of the particulate flow we had chosen the initial average particle velocity. So I now may substitute $V_s(y_0) = V_0$,

$$C(y)/C_0 = (V_s(y)/V_0)(V_0/V(y))$$

$$C(y)/C_0 = V_s(y)/V(y)$$

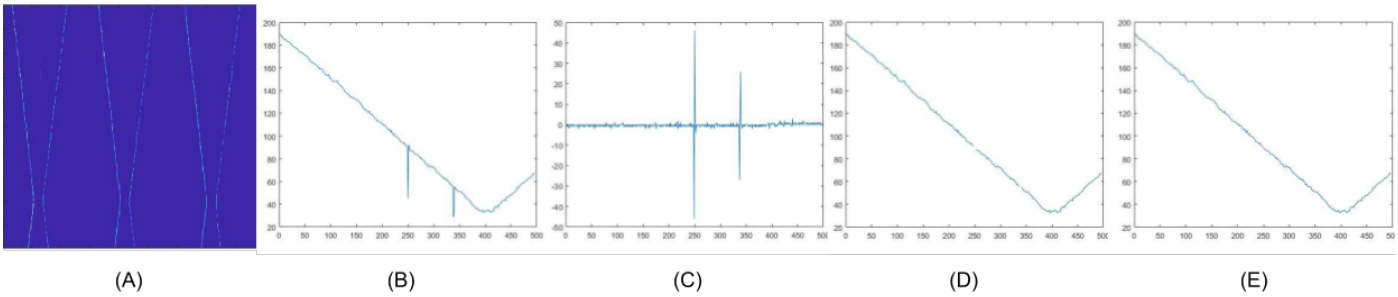

Figure 14: (A) We took a derivative of the minimum channel image and thresholded brightness to isolate the edges. (B) For each channel, we found the difference between consecutive edges. Missing pieces of the edges causes drastic errors. (C) Errors are (D) eliminated by chopping off points were the deivative of the width function exceeds a small threshold. (E) Fitting a linear interpolation to the channel provides a rough function for the width of the channel versus y-position.

We now have a model of particle concentration as a function of the ratio of the predicted simple fluid average velocity over the measured average particle velocity. Comparing the predicted particle concentration from this model to the actual concentration shows good correlation, spare the anomaly at the cusp of the channel throat brought on by the aforementioned drop in particle velocity below the simple fluid model prediction. The concentration data shows a decline in concentration towards the channel throat (Figure 16).

Another metric for determining how particle spacing is affected by flow through a constriction is nearest neighbor proximity. To get an estimate of how spread out the particles are at different y-points in the channel, I analyzed the frames of our flow footage to get the average distance to the to the nearest neighbor and binned the results by y-position. At the extremities of the analysis region results became artificially inflated due to the fact that our program does not see the particles present just beyond the outlet or just behind the inlet. This artificial inflation completely subsides at about 50 μm into the analysis region from either side. The resulting nearest neighbor distance plot shows an increase in the average nearest neighbor distance approaching the throat at y=400 (Figure 17). The rise in nearest neighbor distance does not drop off appreciably after the particles exit the throat, though

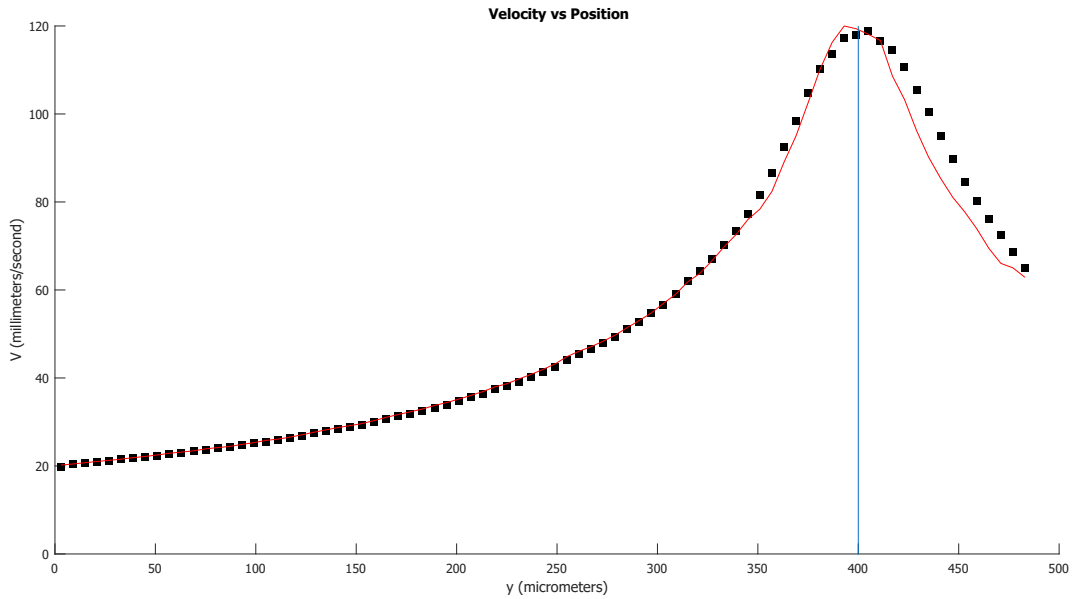

Figure 15: Velocity of the particles (black squares) slightly overtakes the predicted velocity based on the simple fluid model (red) near the throat of the channel at y = 400.

it may return to the initial value when the flow completely exits the channel constriction to join the main outlet flow of the microfluidic device, which would be interesting to test for using a lower scope magnification.

In addition to experimental testing, one goal of this project was to begin developing a computational simulation for clogging. Such a model, though difficult to implement, would be an excellent tool for studying clogging, with the capacity to replicate months worth of experimentation within minutes. A simulation would also allow easy variation of channel geometry and flow properties. To simulate particle flow in a low Reynolds number regime, we use the force coupling method with the incompressible Navier-Stokes equations (Sune Lomholt, 2003). This method allows the carrier fluid to fill the entire flow domain, so particle velocity is calculated as the average of the local fluid velocity enclosed by the surface of the particle. The influence of the particles on the motion of the fluid is modelled as a contribution to the body force term in the Navier-Stokes equations. The force of each particle is modelled

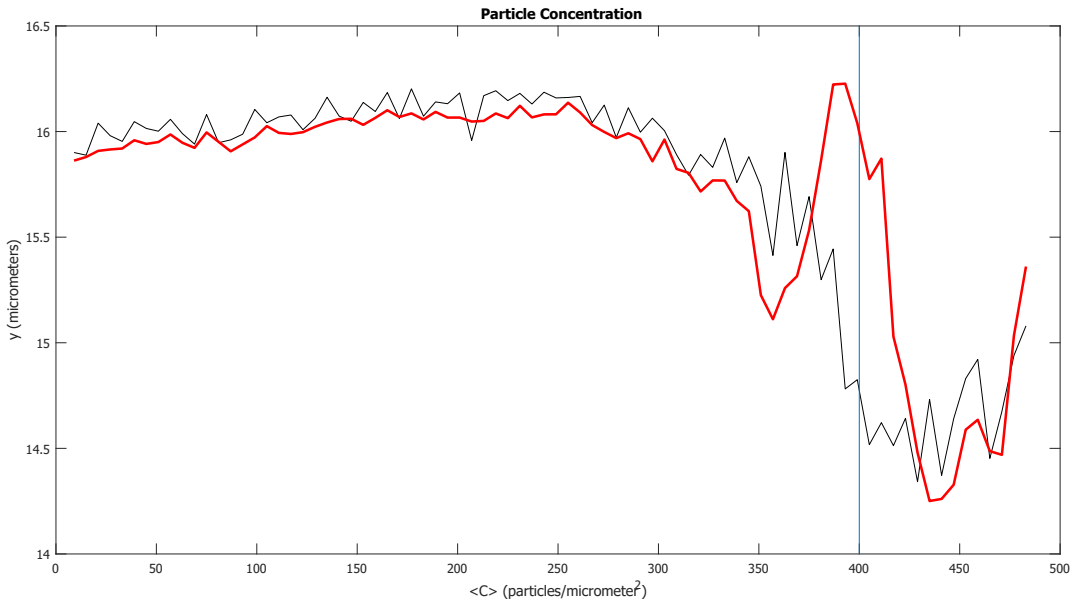

Figure 16: Particle concentration (black) with a prediction (red) based on the discrepancy between the simple incompressible fluid model and the measured particle velocity.

as a lower order force multipole expansion, for which I've used a dipole expansion of a gaussian distribution (Martin Maxey, 2001).

My first version of the simulation simply found the steady state flow field in a 2D channel constriction. This is accomplished using Chorin's projection method to solve the finite difference formulation of the incompressible Navier-Stokes Equations on a cartesian mesh. For boundary conditions at the channel walls I used the homogeneous Neumann condition for pressure normal to the wall and the no-slip condition for velocity. At the the inlet and outlet I used homogeneous Neumann conditions for velocity, and for pressure I set a Dirichlet value at the channel inlet and a non-homogeneous Neumann condition at the outlet. Given an initial velocity field guess of random values, the algorithm converges to an accurate flow field within about 25 iterations.

Having successfully modelled 2D Stoke's flow, I implemented the force coupling method by re-introducing the body force term into the convection equation. When the flow field

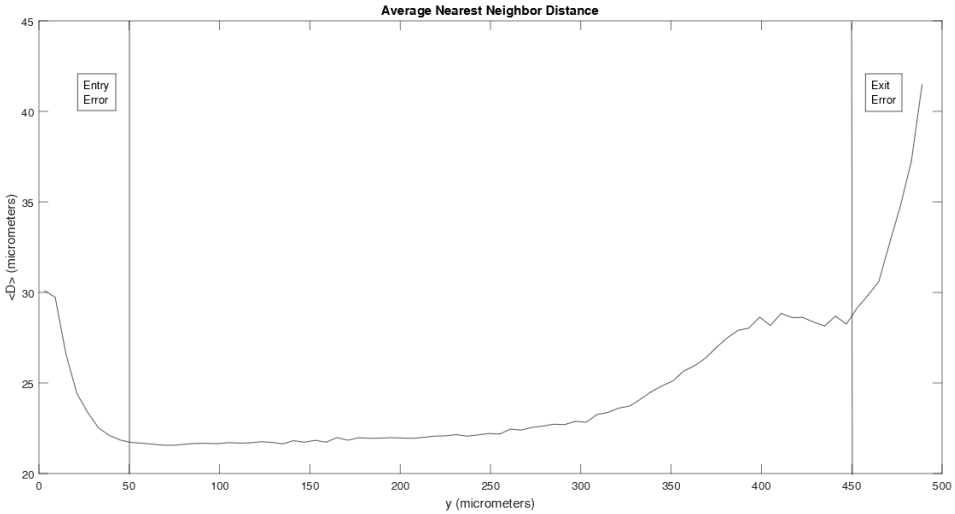

Figure 17: Average nearest neighbor distance increases as the flow enters the constriction, peaking at the throat. The extremities of the graph should be ignored, as they are artificially inflated by the inability of the particle locating algorithm to see beyond the scope of the analysis region.

converges for the empty channel, particles are added, their local body force represented by a Gaussian dipole oriented in the direction of the flow. The resulting flow field successfully forms a stokeslet around the particle (Figure 18). Introducing a model for particle interactions and wall interactions in densely packed states would allow this simulation to reproduce clogging and open up the door for a more thorough study. Creating a simulation which adequately deals with dilute particle flow and packed particle interactions is a tall order, but will greatly benefit future studies.

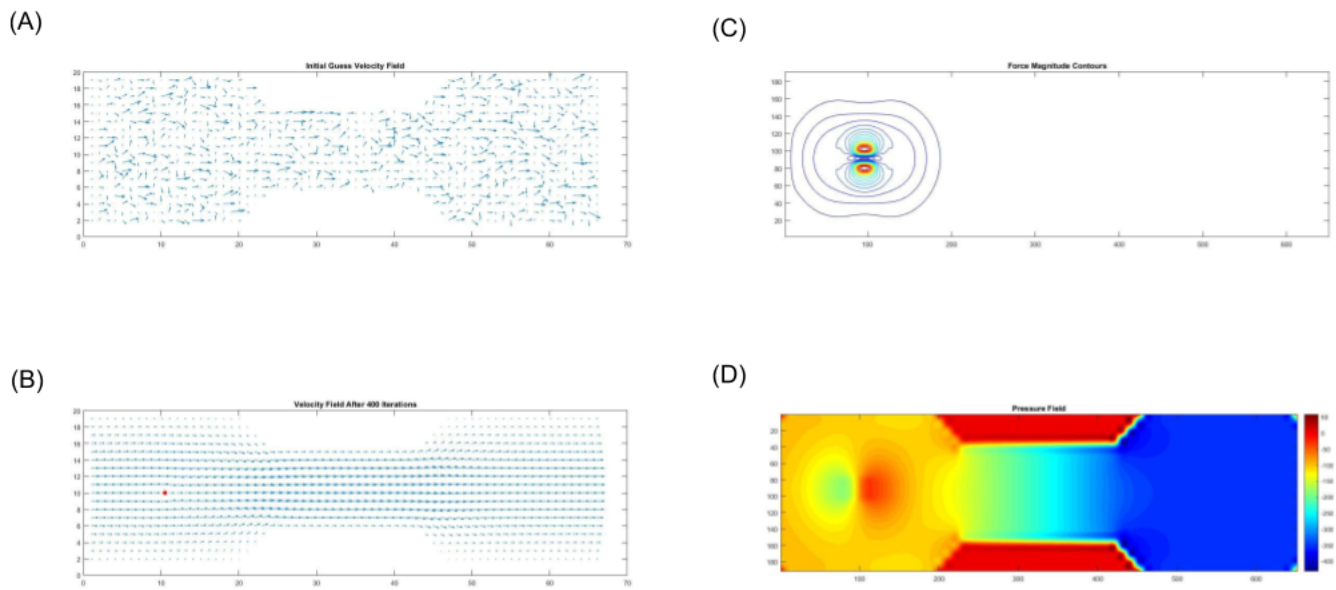

Figure 18: (A) The simulation begins with a random velocity field. (B) A particle is added after flow field converges. (C) Contours showing the shape gaussian dipole force field around the particle. (D) Affect of body force on fluid pressure.

5 Results

Our research was successful in observing the formation of a clog in low Reynolds number two-phase flow. In none of our experiments did we see evidence of a dilute-to-dense flow transition, and the two true clogs which we did record formed by particle assembly into an arch across the throat of the channel constriction. Bulk particle tracking further revealed that the concentration of particles decreases leading up to the channel constriction, accompanied by an increase in the average nearest neighbor interparticle distances. Together these results indicate that the dilute-to-dense transition observed in granular flow jamming does not occur in low Reynolds number clogging. In fact, particle flow becomes even more dilute as the flow area decreases.

Correlation between the growth of a secondary peak in the particle velocity distribution and the increasing difference between the measured average particle velocity and the simple incompressble fluid model prediction strongly suggests that steric exclusion at the channel

wall is responsible for increasing the average particle velocity beyond the limit set by the incompressibility constraint (the connection between steric exclusion and a bimodal velocity distribution is already well known). From the conservation of particle flux, we developed a predictive model for particle concentration as a function of the discrepancy between the simple incompressible fluid model average velocity prediction and the measured average velocity:

$$C(y)/C_0 = V_s(y)/V(y)$$

This model accurately predicted the measured particle concentration change (Figure 16). Since this model is based off an effect likely resulting from steric exclusion at the channel walls, which forces particles into a higher velocity flow region, it follows that steric exclusion is the most likely cause for the decrease in particle concentration as the channel constriction narrows.

The velocity-time graphs for the clogging particles show relatively unimpeded flow prior to clogging, and then immediate simultaneous stoppage. This simultaneous halting reinforces what can clearly be seen from the clogging image sequences (Figure 8): particles in low Reynolds number flow with minimal particle-particle and particle-wall sticking clog due to the happenstantial configuration of particles into an arch as they are drawn towards the throat, without prior dilute-to-dense flow transition.

6 Discussion

This research represents an initial exploration of clogging, and as such raises new questions. What is the nature of clogging probability dependence on particle concentration? What other factors are involved? Would flow concentration occur for high enough friction between the particles and the channel walls? Truly, the door is open for more experimentation to be conducted and for us to begin developing a theory of clogging.

A good starting point is to further verify the relations uncovered by our analysis. From our central idea that clogging probability is dependent upon local particle concentration, we can use our result that steric exclusion is responsible for changes in particle concentration to make some predictions for the effect of geometry on clogging susceptibility. If we were to take our channels with the same tapering pitch and throat width and extend the inlet such that the mouth of the constriction is wider, we would increase the effect of steric exclusion because a greater proportion of the particles flowing into the channel mouth will become confined to the channel wall. Such a change should, according to our results, serve to further lower the local particle concentration at the channel throat and hence further reduce clogging probability. Interestingly, this exact phenomena was observed by Weitz's group, who found that clogging was less likely to occur in channels with large mouths. Though they accounted for this effect by conjecturing that the increase in shear stress destabilizes clot formation, it would seem based on our results that the effect would hold true for non-clotting flow as well. Testing this argument by experimenting with various constriction ratios is a tractable next step in our clogging research.

The results of this project have immediate implications in modern fluid mechanical and chemical engineering. Many robotic systems use extremely narrow oil lines which lend themselves to low Reynolds number flows. If engineers could optimize their designs to induce steric exclusion in regions where flow constriction is necessary, they could reduce the chance of line clogging. For fine filtration systems, such as those involved in water desalination, pore constriction ratio can be another factor in determining how to minimize clogging susceptibility. The potential applications of clogging research will increase as clogging theory extends to encompass a broader range of fouling phenomena.

7 Acknowledgments

I would like to thank my research advisers, Timothy Atherton and Jeffrey Guasto, for their continued support throughout this project and for access to a wealth of technological and intellectual resources that they provided to me. I would also like to thank my peers in Jeffrey Guasto's microfluidics lab group, who played a major role in helping with the microfluidic device fabrication process and in training me to use various laboratory equipment, and Timothy Atherton's soft matter theory group, who advised my methods in research and simulation building. I am especially grateful for my collaboration with fellow undergraduate student Thomas Coons, who worked on this project with me over the summer to refine our experimental methods. Lastly, I would like to thank the Tufts Summer Scholar committee and my research sponsor Steven Eliopoulos; this project would not have succeeded without their funding.

References

[1] Lomholt, S., & Maxey, M. R. (2003). Force-coupling method for particulate two-phase flow: Stokes flow. *Journal of Computational Physics*

[2] Maxey, M. R., & Patel, B. K. (2001). Localized force representations for particles sedimenting in Stokes flow. *International Journal of Multiphase Flow*

[3] Zeta-Meter inc. Zeta Potential: A Complete Course in 5 minutes. Retrieved from www.zeta-meter.com

[4] Weitz, D. A., Massenburg, S. S., & Amstad, E. (2016). Clogging in Parallelized Tapered Microfluidic Channels. Retrieved from www.springer.com

[5] Kiwing, T. (2005). Jamming transition in two-dimensional hoppers and silos. *American Physical Society*

[6] Zhong J., Hou, M., Shi, Q., & Lu, K., (2006). Criticality of the dilute-to-dense transition in a 2D granular flow. *Journal of Physics: Condensed Matter*

[7] Vaziri Hassas, B. (2013). Effect of hydrophilic lipophilic balance (HLB) of nonionic surfactants on ultrafine lignite dewatering. 10.13140/RG.2.1.3600.8721.

[8] Fletcher, Clive A. J. *Computational Techniques for Fluid Dynamics.* New York: Springer-Verlag Berlin Heidelberg, 1988. Print.

[9] Hamaker, H. C. (1937). The London-Van Der Waals Attraction Between Spherical Particles. *Physica IV*